DOI: 10.1002/ejic.200900991

Hydrangea-Like Meso-/Macroporous ZnO-CeO_2 Binary Oxide Materials: Synthesis, Photocatalysis and CO Oxidation

Tian-Yi Ma,[a] Zhong-Yong Yuan,*[a] and Jian-Liang Cao[a]

Keywords: Mesoporous materials / Zinc / Cerium / Heterogeneous catalysis / Oxidation

A series of ZnO-CeO_2 binary oxides with a novel hydrangea-like morphology and meso-/macroporous hierarchical structure of high surface area (around 100 m^2/g) were synthesized by a simple one-pot hydrothermal process in the presence of triblock copolymer F127. Homogeneous mixing of wurtzite ZnO and cubic phase CeO_2 and the coexistence of Ce^{3+} and Ce^{4+} on the surface of the synthesized ZnO-CeO_2 materials were confirmed. UV/Vis diffuse reflectance spectra show that the absorption edges of the binary oxides shift remarkably to the visible range relative to those of pure ZnO and CeO_2. Their photoactivities were tested by photodegradation of Rhodamine B under UV and visible light irradiation, and excellent photocatalytic performance for organic waste degradation was found in the synthesized hydrangea-like meso-/macroporous ZnO-CeO_2 materials. Furthermore, their application as heterogeneous catalysts for CO removal was evaluated, and the results indicate that the synthesized ZnO-CeO_2 materials exhibit efficient activity for removing CO by catalytic oxidation, demonstrating a promising potential in environmental remediation.

Introduction

Recent works have focused on the designed synthesis and exploration of applications of binary oxide films or powders, such as TiO_2-CeO_2,[1] TiO_2-ZnO,[2] TiO_2-SiO_2,[3] and TiO_2-WO_3,[4] which were considered to be effective semiconductors, advanced materials, heterogeneous catalysts, and catalyst supports. Physically mixing two or more phases of nanoparticles[5] and chemical synthesis by various synthetic routes[6,7] are two general strategies to fabricate multicomposites. The chemical synthesis method allows a better mixing and closer contact among the different phases,[8] normally with nanoporous structures,[9,10] nanorods,[8] or core/shell structures,[11] etc. It is generally accepted that the properties of the composites obtained often cannot be considered as a simple superposition of the properties of individual components because of strong surface interactions between the closely packed nanoparticles in binary oxide systems.[8,10] Thus, combining the advantages of the different phases to obtain a further improvement and wider applications has always been the aim of the synthesis of multicomponent materials.[12]

Zinc oxide (ZnO), an important II–VI semiconductor with a band gap value of 3.37 eV and a large exciton binding energy of 60 meV, has been extensively used as a photocatalyst, sometimes reported to be more efficient than TiO_2 for the photooxidation of phenol and nitrophenols.[13,14] The wide application of CeO_2 in heterogeneous catalysis is mainly due to two features of CeO_2: the redox couple Ce^{3+}/Ce^{4+} and the high capacity to store oxygen.[15] CeO_2-doped TiO_2 and CeO_2-TiO_2 mixed photocatalysts responding to UV or even visible light were reported.[16,17] Moreover, ZnO and CeO_2 were also used as components of heterogeneous catalysts or catalyst supports for catalytic oxidation reactions,[18,19] though reports on the synthesis and applications of coupled bicomponent ZnO-CeO_2 materials are scarce.

The incorporation of macrovoids or macropores into mesoporous materials may be somewhat interesting and useful for catalysis and for engineering pore systems, because one of the potential applications for manipulated, mass-manufactured hierarchical materials with different pore sizes integrated in one body is to combine reduced resistance to diffusion and high surface areas, yielding improved overall reaction and adsorption/separation performances, which can be extended to biological applications.[20] The macropores could be created with the use of either hard or soft templates, such as colloidal crystals,[21] emulsions,[22] and polymers,[23] as well as by a spontaneous process in the absence of any surfactants.[24] On the basis of our previous work on the hierarchical meso-/macroporous metal oxides and metal phosphates,[25–27] hydrangea-like ZnO-CeO_2 mesoporous materials were synthesized in the presence of triblock copolymer F127. The hydrangea structure was covered with irregular macrovoids, which exhibited high photocatalytic activity in the photodecomposition of Rhodamine B (RhB) and was also proved to be an efficient catalyst for CO oxidation.

[a] Institute of New Catalytic Materials Science, Key Laboratory of Energy-Material Chemistry (Tianjin) and Engineering Research Center of Energy Storage and Conversion (Ministry of Education), College of Chemistry, Nankai University, Tianjin 300071, People's Republic of China
Fax: +86-222-3509610
E-mail: zyyuan@nankai.edu.cn

Supporting information for this article is available on the WWW under http://dx.doi.org/10.1002/ejic.200900991.

Results and Discussion

Material Synthesis and Characterization

Triblock polymer F127 was employed as the surfactant, and $Ce(NO_3)_3{\cdot}6H_2O$ and $Zn(NO_3)_2{\cdot}6H_2O$ were used as inorganic precursors. The pH value of the final reaction solution was adjusted to 9–10 by dropwise addition of aqueous NaOH solution in order to co-precipitate Ce^{3+} and Zn^{2+} ions and form a coupled mixed oxide. Hydrothermal treatment was performed in a Teflon-lined autoclave at 110 °C for two days. All of the surfactant species in the pore channels of the obtained materials could be removed by calcination at 500 °C for 3 h in air. Figure 1 shows several representative SEM images of the synthesized ZnO-CeO_2 samples. In the low-magnification images (Figure 1a and b), high-yield hydrangea-like clusters of the mixed oxides with an average diameter of 4–5 μm can be observed. A closer observation (Figure 1c and d) shows that each cluster is covered with many macropores or macrovoids with irregular shapes and sizes, which resemble the previously reported macroporous lanthanide–organic coordination polymer foams[28] with similar morphologies but on much larger scales. The morphology did not change a lot during the calcination process (Figure S1 in the Supporting Information). However, only elliptic nanoparticles and disordered nanosheets could be seen in the SEM images of pure ZnO and pure CeO_2 (Figure S2 in the Supporting Information), which are quite distinct from the morphology of the synthesized binary ZnO-CeO_2.

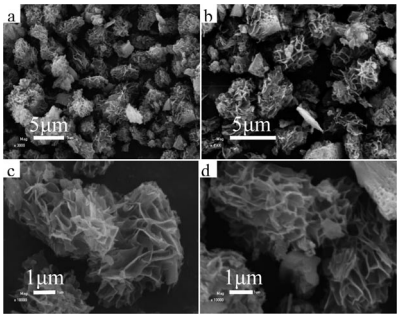

Figure 1. SEM images of Ce50Zn50.

The particulate morphology of binary ZnO-CeO_2 oxides is confirmed by the TEM images (Figure 2). Tightly aggregated nanoparticles present pieces of stacked nanosheets (Figure 2a), which construct the petals of the hydrangea and also the pore wall of the macropores. As one can see in Figure 2b, the macropore walls are composed of nanoparticles with a uniform size of 4–6 nm, which present interparticle mesoporosity without long-range order. The high-resolution images (Figure 2c) further confirm that the walls of the macroporous network were composed of accessible mesopores with a wormhole-like array, in which the lattice fringes of the mixed ZnO-CeO_2 can be observed clearly, reflecting the crystalline phase of the nanoparticles. Combined with the observation of the hydrangea-like microstructure in the SEM images, the novel hierarchical structure of the synthesized binary ZnO-CeO_2 oxides was confirmed.

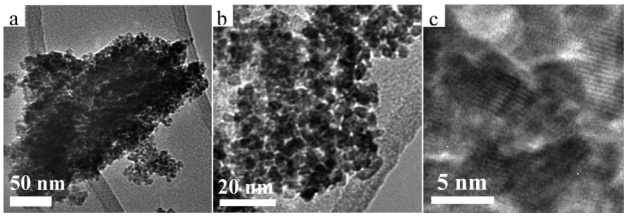

Figure 2. TEM images of Ce50Zn50 (a) and Ce60Zn40 (b, c).

The nitrogen adsorption/desorption isotherms of the synthesized samples and their corresponding pore-size distributions are shown in Figure 3; their textural properties are listed in Table 1. The isotherms of pure CeO_2 are of type IV and characteristic of mesoporous materials, according to the IUPAC classification. The isotherms of the mixed oxides (Ce60Zn40, Ce50Zn50, Ce40Zn60) are between type IV and type II. An increase in the volume of nitrogen adsorbed at high relative pressure ($P/P_0 > 0.8$) can be observed on the isotherms of mixed ZnO-CeO_2 materials, which is similar to the previously reported materials with hierarchical structure,[25–27] indicating an appreciable amount of macroporosity. This is in agreement with the SEM images shown in Figure 1. The hysteresis loop of pure CeO_2 has a triangular shape and a steep desorption branch, which belongs to type H2 hysteresis.[29] Such behavior was attributed to pore connectivity effects,[29] which were often considered to be a result of the presence of pores with narrow mouths (ink-bottle pores). The hysteresis loops of mixed ZnO-CeO_2 materials are basically close to those typical of type H2, indicating interconnected mesopores.[29] This conclusion is supported by the TEM images (Figure 2). The mixing of ZnO with CeO_2 and the presence of the macropores could alter the adsorption/desorption behavior of the coupled ZnO-CeO_2 oxides to something slightly like type H3 loops. One single but ill-defined peak with a maximum at 1.7–3.2 nm was observed in the pore-size distribution curves of the samples (Figure 3b). This porosity should be a result of the organized aggregation of mixed ZnO-CeO_2 nanoparticles that were the hydrolysis products of $Ce(NO_3)_3$ and $Zn(NO_3)_2$ in F127 solution. It is interesting to note that the surface area, pore size, and pore volume of the mixed ZnO-CeO_2 samples were all enlarged with the increase in cerium content. Sample Ce60Zn40 possesses the largest surface area (113 m^2/g), which is even larger than that of pure CeO_2. The pure ZnO sample has a limited adsorption volume of nitrogen with very small surface area and pore volume. Since the Barret–Joyner–Halenda (BJH) method somewhat underestimates small mesopores, DFT modeling was also used to calculate the pore sizes of the materials (Figure S3 in the Supporting In-

Table 1. Summary of the physicochemical properties and photocatalytic rate constants of the synthesized CeO_2-ZnO materials.

Sample	Crystal size[a] [nm]	S_{BET}[b] [m^2/g]	$D_{BJH\text{-}ads}$[c] [nm]	D_{ave}[d] [nm]	V_{pore}[e] [cm^3/g]	D_{DFT}[f] [nm]	T_{100}[g] [°C]	Band gap [eV]	Photodegradation rate constant k [min^{-1}]	
									UV light	Visible light
Ce60Zn40	4.9	113	3.2	6.7	0.19	6.3	270	2.62	0.02669	0.00705
Ce50Zn50	5.2	101	2.7	6.5	0.16	7.1	290	2.72	0.02278	0.00642
Ce40Zn60	4.4	90	2.2	6.8	0.14	6.0	300	2.78	0.01624	0.00536
CeO_2	8.2	98	2.5	5.2	0.15	6.8	355	3.35	0.00338	0.00107
ZnO	13.2	7	1.7	3.3	0.02	4.7	>380	3.08	0.00461	0.00166

[a] Calculated by the Scherrer formula. [b] BET surface area calculated from the linear part of the 10-point BET plot. [c] Estimated by using the adsorption branch of the isotherm by the BJH method. [d] BJH average pore size (4V/A). [e] Single-point total pore volume of pores at $P/P_0 = 0.97$. [f] Pore diameters calculated by the DFT method. [g] Temperatures for total conversion of CO by the synthesized catalysts.

formation), and pore-size distributions of around 6.3, 7.1, and 6.0 nm were obtained for Ce60Zn40, Ce50Zn50, and Ce40Zn60, respectively, which are also listed in Table 1 for comparison.

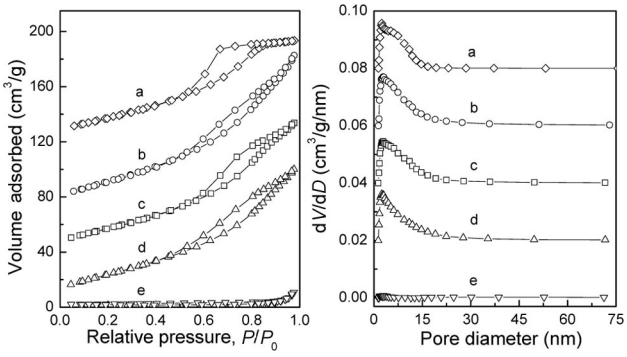

Figure 3. N_2 adsorption/desorption isotherms (left) and the corresponding BJH pore-size distribution curves (right) of synthesized samples: (a) CeO_2, (b) Ce60Zn40, (c) Ce50Zn50, (d) Ce40Zn60, and (e)ZnO. The adsorbed volume was shifted by 110, 60, and 30 units for the curves of data sets a, b, and c, and the dV/dD value was shifted by 0.08, 0.06, 0.04, and 0.02 units for the curves of data sets a, b, c, and d, respectively.

Figure 4 shows the XRD patterns for the coupled ZnO-CeO_2 materials, which provide further insight into the crystallinity of the products. Monocomponent materials were confirmed to be wurtzite ZnO and cubic phase CeO_2 with crystal sizes of 13.2 and 8.2 nm, respectively, as calculated by the Scherrer formula (Table 1). Relative to the monocomponent nanomaterials, the coupled nanocomposites indeed consist of both wurtzite ZnO and cubic phase CeO_2, and the characteristic peaks of wurtzite ZnO gradually decrease with the increase in the Ce/Zn molar ratio (from 2:3 to 3:2), while the characteristic peaks of cubic phase CeO_2 gradually increase. This suggests the successful preparation of the coupled bicomponent nanocomposites consisting of cubic phase CeO_2 and wurtzite ZnO. The crystal sizes of the mixed oxides dramatically fall to around 5 nm as compared with those of pure ZnO and CeO_2, which is in agreement with the TEM observation (Figure 2).

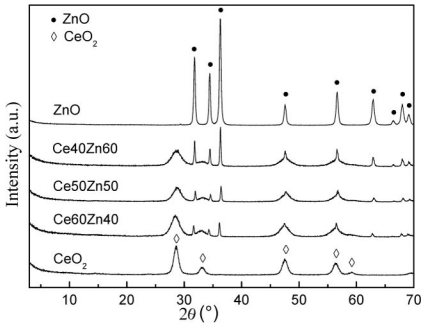

Figure 4. XRD patterns of the synthesized samples.

Considering the results of SEM, TEM, N_2 sorption, and XRD analysis, the formation mechanism of the hydrangea-like meso-/macroporous ZnO-CeO_2 binary oxides was proposed in Figure 5, which is directly based on the formation mechanism of monocomponent ZnO and CeO_2 oxide. As to pure ZnO oxide (route 1), the hydrolysis of the Zn-$(NO_3)_2$ in F127 solution leads to the formation of relatively large ZnO nanoparticles with a diameter of about 13 nm (calculated from XRD results). From N_2 sorption analysis, the pure ZnO sample has limited adsorption volume of nitrogen with very small surface area and pore volume, which is similar to some reports,[30,31] indicating the weak interactions between the surfactant and inorganic species. Although the F127 molecules failed to play a role as the surfactant, the interfacial polymerization of ZnO particles around the microemulsion drops composed of H_2O, C_2H_5OH, and F127 micelles still happened, resulting in the elliptic morphology.[30,31] The hydrolyzed products of $Ce(NO_3)_3$ were of smaller diameter, and the interactions between organic and inorganic species were stronger,[32] making F127 molecules possible surfactants during the formation process of mesoporous CeO_2. Thus, the resultant monocomponent CeO_2 was characteristic of mesoporous material with high surface area (98 m^2/g), which was confirmed by the N_2 sorption measurement. Like other reported ceria materials,[33] CeO_2 with only an isolated layered or plate-like microstructure was obtained, because the interfacial microemulsion polymerization did not happen here (route 3). On the basis of the formation mechanism of the above-

mentioned elliptic ZnO and layered CeO_2, the generation of the present hydrangea-like meso-/macroporous ZnO-CeO_2 binary oxide could be regarded as the collaborative result of the organic surfactant effect and the microemulsion polymerization procedure (route 2). The hydrolysis of the $Ce(NO_3)_3$ and $Zn(NO_3)_2$ precursors in an aqueous solution of F127 would result in the rapid formation of nanometer-sized (smaller than the sizes of hydrolyzed ZnO and CeO_2) mixed oxide sols, which could react with F127 molecules to form nanoparticles of surfactant/ZnO-CeO_2 composites with a large number of surface hydroxy groups due to incomplete condensation. Meanwhile, the surfactant molecules in solution could be adsorbed onto the surface of these primary nanoparticles, and further self-assembling of these composites could take place to form the so-called mesostructures. The hydrangea-like microstructures covered with irregular macropores or macrovoids were generated by interfacial microemulsion polymerization. As a generally accepted conclusion of the generation of macropores, the colloidal crystal hard templates usually lead to the formation of three-dimensional ordered macropores,[21,34] and the microphase separation process often creates one-dimensional orientation and uniform macrochannels.[25,26] Furthermore, the microemulsion droplets induced by stirring can be used to template the nonuniform or spherical macropores,[22,35,36] which could be the direct cause of the present hydrangea-like macropores. The microemulsion drops composed of H_2O, C_2H_5OH, and F127 micelles were formed under mild stirring, and because the emulsion drops are deformable, micrometer-scaled architectures were able to accommodate stresses that arise during gelation and shrinkage. However, porous materials made using rigid spheres, by contrast, tend to break into small pieces that are seldom larger than several micrometers.[36] Then, the polymerization of mesostructured ZnO-CeO_2 sols surrounding the emulsion drops enabled the formation of the three-dimensional hydrangea architecture, instead of the isolated layered structure. Thus the surfactant F127 molecules not only assist the formation of micrometer-scaled emulsions, which have created the hydrangea morphology, but also direct the generation of mesostructure among the petals.

The thermogravimetry-differential scanning calorimetry (TG-DSC) profiles of the as-prepared Ce40Zn60 solid show a continuous weight loss of 32.9% from 25 to 500 °C (Figure 6). The weight loss of 8.7% from 25 to 220 °C, accompanied by an endothermal peak at around 100 °C, can be attributed to desorption of the adsorbed and intercalated water molecules, and the weight loss of 24.2% from 220 to 500 °C, accompanied by an exothermic peak at around 380 °C, can be attributed to decomposition of the organic surfactant F127 and the combustion of carbon species. No crystalline phase transformation is observed. After 500 °C, the weight of the precursor no longer changes, which indicates that the carbon species (surfactant molecules) in the samples had been completely removed by calcination at 500 °C in air. Since calcination at high temperature could result in a decline in the surface area and an increase in the crystallite size of catalysts, the feasible calcination temperature under an atmosphere of air is 500 °C for the ZnO-CeO_2 catalysts.

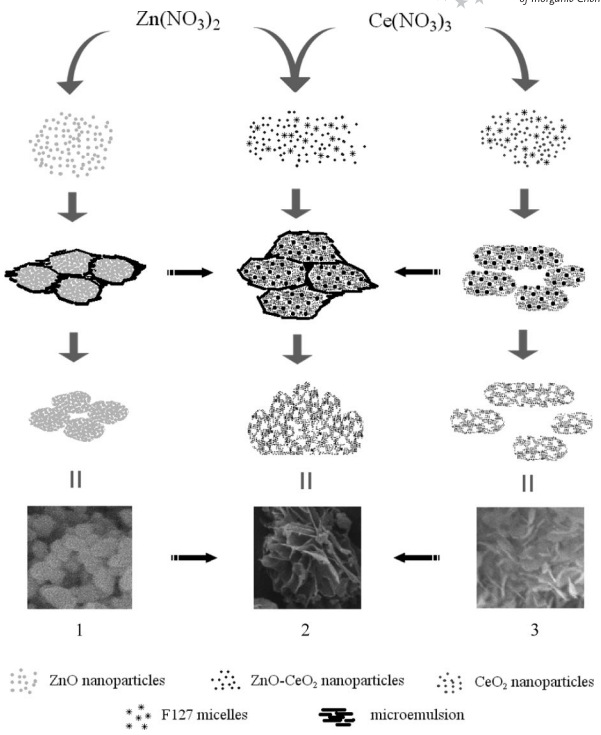

Figure 5. Formation mechanism of the synthesized materials.

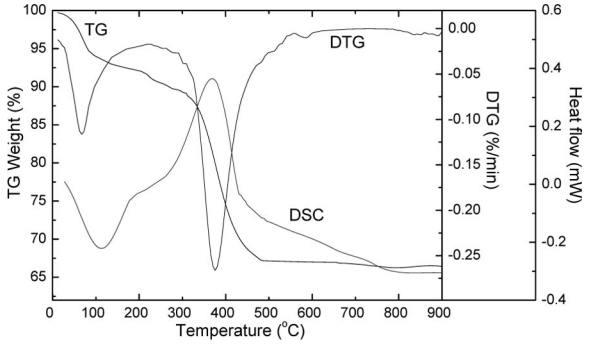

Figure 6. TG-DSC profiles of the as-prepared Ce40Zn60 solid.

Figure 7 shows the high-resolution XPS spectra of O 1s, Zn 2p and Ce 3d, taken on the surface of the Ce50Zn50 sample, which are collected to study the surface chemistry of the synthesized catalysts. The XPS spectrum of O 1s was asymmetric, indicating that at least two kinds of oxygen species were present on the surface. The dominant peak at about 529.1 eV is characteristic of metallic oxides, which is in agreement with the O 1s electron binding energy arising from the ceria and zinc oxide lattice.[37,38] Another shoulder peak at 531.2 eV is due to surface hydroxyl groups. As to the XPS spectrum of Zn 2p, the spin-orbit component ($2p_{3/2}$ and $2p_{1/2}$) of the peak is well deconvoluted by two curves at approximately 1021.7 and 1045.1 eV respectively, corresponding to ZnO.[38] The XPS spectrum of Ce 3d is rather complex and can be assigned to $3d_{3/2}$ spin-orbit

states (labeled u) and $3d_{5/2}$ states (labeled v). However, a straight interpretation of the spectrum is possible by following the intensity of the marked peaks in the Figure 7. The u′′′/v′′′ doublet is due to the primary photoemission from Ce^{4+}-O_2. The u/v and u′′/v′′ doublets are shakedown features resulting from the transfer of one or two electrons from a filled O 2p orbital to an empty Ce 4f orbital. The u′/v′ doublet is due to photoemission from Ce^{3+} cations.[16,17] The Ce 3d spectrum of the ZnO-CeO_2 sample basically denotes a mixture of $Ce^{3+/4+}$ oxidation states giving rise to a myriad of peaks, indicating the coexistence of Ce^{3+} and Ce^{4+} in ZnO-CeO_2 materials and pointing out the fact that the surface of the sample is not fully oxidized. The surface atomic composition of the Ce50Zn50 sample was calculated as 16.80% Zn, 18.95% Ce, and 64.16% O. The Zn/Ce ratio is almost 1:1, suggesting compositional homogeneity throughout the coupled ZnO-CeO_2 materials.

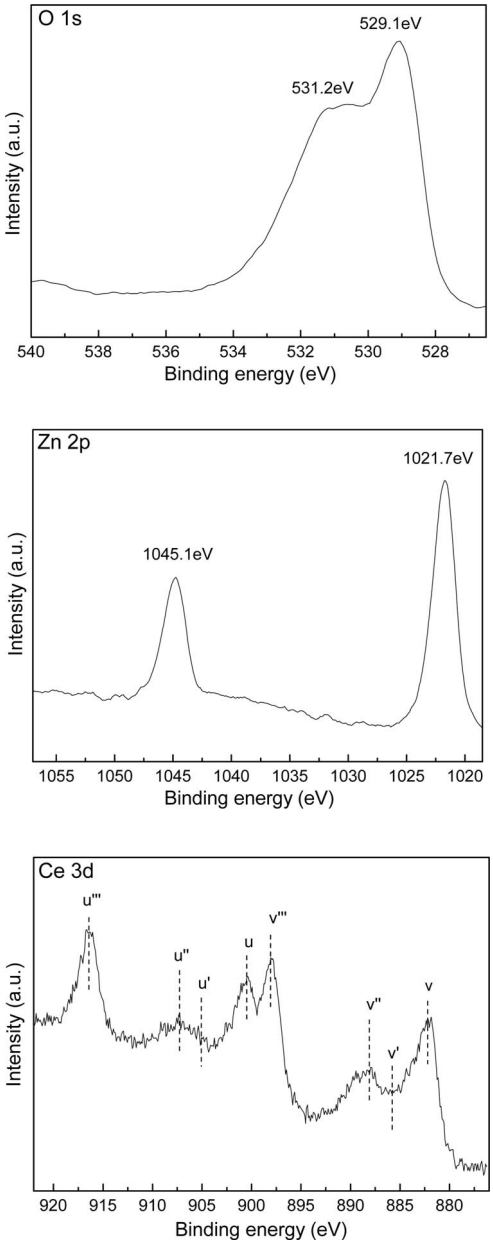

Figure 7. High-resolution XPS spectra of the O 1s, Zn 2p and Ce 3d regions of the sample Ce50Zn50.

Photocatalytic Activity

It is well known that ZnO can be used as a semiconductor photocatalyst for the photoreductive dehalogenation of halogenated benzene derivatives, the photocatalytic degradation of water pollutants, and the photocatalytic reduction of toxic metal ions.[13,14] Through the photocatalytic generation of hydrogen peroxide, ZnO can be utilized for the degradation of organic pollutants in nearly neutral solutions and for the sterilization of bacteria and viruses.[39] However, as a widely used photocatalyst, ZnO requires only the near-UV light to activate its attractive photocatalytic properties. Some hierarchically structured ZnO nanoparticles with high surface areas[39,40] have been reported to possess promoted UV photocatalytic activities, though their visible light photocatalytic activities were seldom accessed.

The UV/Vis diffuse reflectance spectra of coupled ZnO-CeO_2 materials are presented in Figure 8. The strong absorption in the UV region (200–400 nm) is the characteristic of ZnO, and the absorption in the region 200–300 nm is the characteristic of CeO_2. The absorption edges of the mixed oxides (446.5 nm for Ce40Zn60, 456.7 nm for Ce50Zn50, and 472.4 nm for Ce60Zn40) shift to the visible range remarkably. The band gap value of the samples is calculated by the formula E_g (eV) = 1240/λ_g (nm), where λ_g stands for the wavelength value corresponding to the intersection point of the vertical and horizontal parts of the spectra, and a narrowing of the band gap value is observed with an increase in cerium content (3.08 eV for ZnO, 2.78 eV for Ce40Zn60, 2.72 eV for Ce50Zn50, and 2.62 eV for Ce60Zn40), but pure CeO_2 has the largest band gap value of 3.35 eV (Table 1). The change in the optical absorption behavior of binary oxides was mainly due to the interfacial effects between CeO_2 and ZnO_2 grains, residual carbon species from the synthesis process and the enhanced mesoporosity. The redshift of absorption edges and narrowing of the band gaps, which are observed in the UV/Vis diffuse reflectance spectra, may improve the photocatalytic behavior of the synthesized hierarchical ZnO-CeO_2 materials.

The photocatalytic activities of the mixed oxides were evaluated by photodegradation of RhB under UV light and visible light irradiation (Figure 9); they were compared with those of pure ZnO and pure CeO_2. A blank experiment (self-photosensitized process) was also performed in the absence of any catalysts for comparison. The photocatalytic degradation reaction can be assumed to follow a pseudo-first-order expression: $\ln(C_0/C) = kt$, where C_0/C is the normalized organic compound concentration and k is the apparent reaction rate (min^{-1}). The photocatalytic activity has been defined as the overall degradation rate constant of the catalysts. By plotting $\ln(C_0/C)$ as a function of irradiation time, through regression (Figure 9b and d), the k constant

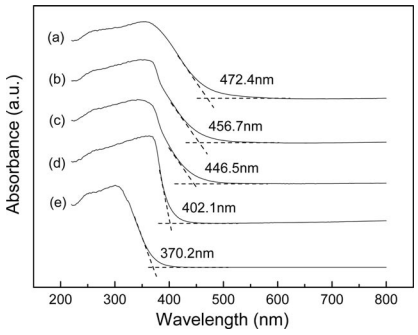

Figure 8. UV/Vis diffuse reflectance spectra of synthesized samples: (a) Ce60Zn40, (b) Ce50Zn50, (c) Ce40Zn60, (d) ZnO, and (e) CeO_2.

from the slopes of the simulated straight lines can be obtained, which is listed in Table 1. Under UV light irradiation (Figure 9a), only a very small degree of photodegradation (9.6%) took place without adding any catalyst, and degradations of 30.23% and 40.24% were performed by pure CeO_2 and pure ZnO, respectively, after 120 min of UV light irradiation, relative to degradations of 98.77%, 96.64%, and 91.43% by Ce60Zn40, Ce50Zn50, and Ce40Ti60, respectively. All of the ZnO-CeO_2 samples exhibit photocatalytic activity superior to monocomponent materials, giving the photoactivity sequence Ce60Zn40 > Ce50Zn50 > Ce40Ti60 (> ZnO > CeO_2). Correspondingly, the reaction rates (shown in Figure 9b) share the same sequence with the photocatalytic activities in Figure 9a. Reaction rates higher than those of CeO_2 (0.00338 min^{-1}) and ZnO (0.00461 min^{-1}) were obtained for all hierarchical ZnO-CeO_2 samples. Similarly, the ZnO-CeO_2 samples were also proved to be better photocatalysts than monocomponent materials under visible light irradiation, with degradations of 57.02%, 54.10%, and 47.32% for Ce60Zn40, Ce50Zn50, and Ce40Ti60 after 120 min of irradiation, respectively, which is much higher than those of pure ZnO (18.5%) and CeO_2 (12.5%). The calculated reaction rates of ZnO-CeO_2 catalysts (Figure 9d) are higher than those of ZnO and CeO_2, too, as listed in Table 1. Under both UV and visible light irradiation, the photoactivites of the synthesized ZnO-CeO_2 samples increase with their cerium content (Ce60Zn40 > Ce50Zn50 > Ce40Zn60 > ZnO), consistent with UV/Vis diffuse reflectance spectra, while pure CeO_2 exhibit the lowest photoactivity.

The higher photocatalytic activity of the hierarchical ZnO-CeO_2 materials could be attributed to the redox couple Ce^{3+}/Ce^{4+} and the high capacity to store oxygen.[15,41] The Ce^{4+} and Ce^{3+} coexisting on the surface of ZnO-CeO_2 photocatalysts, as revealed by XPS analysis, influences the photoreaction by altering the electron–hole pair recombination rate.[15] Ce^{4+} is a scavenger of electrons and easily traps the electron. The electrons trapped in a Ce^{4+}/Ce^{3+} site are subsequently transferred to the surrounding adsorbed O_2, and hence the lifetime of the electron–hole pair is extended. However, the recombination rate of photogenerated electron–hole pairs is much faster without Ce^{4+}/Ce^{3+} sites that trap electrons, and the content of the chemisorbed oxygen

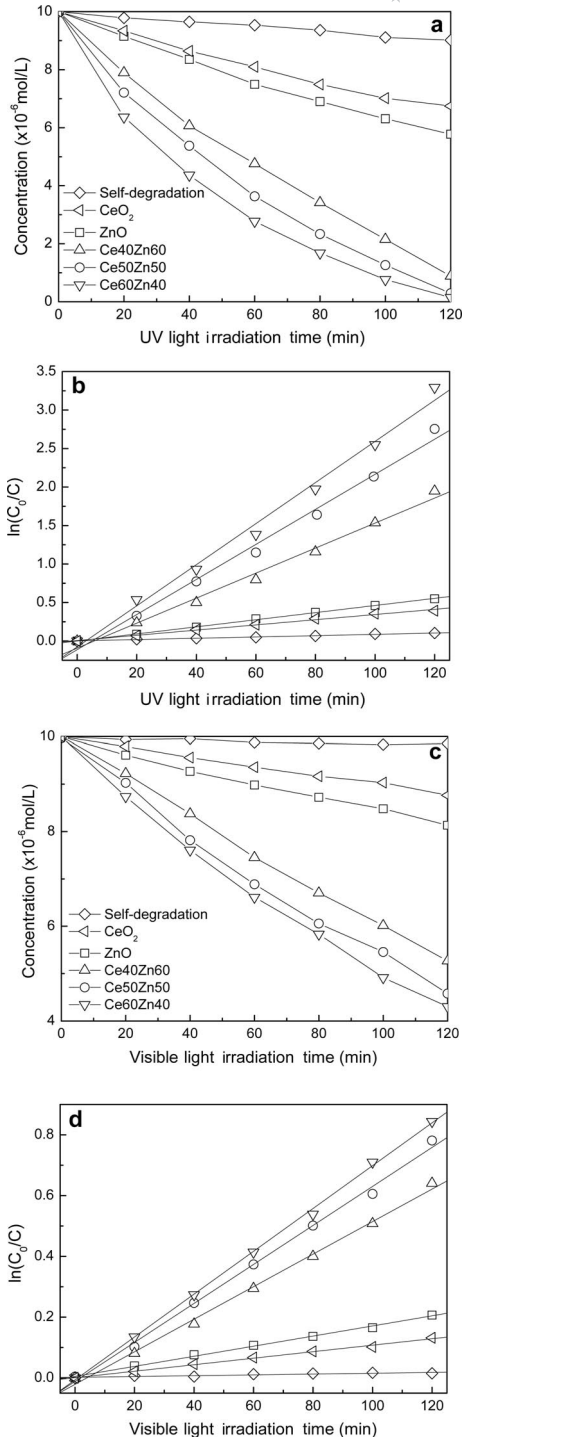

Figure 9. Photocatalytic activities of samples for RhB degradation under UV light (a) and visible light (c) irritation; plots of $\ln(C_0/C)$ vs. the irradiation time for UV light (b) and visible light (d) irradiation, showing the fitting results by using a pseudo-first-order reaction scheme.

is very limited on the surface of pure ZnO, which results in the low photoactivity for pure ZnO. Furthermore, the notable redshift of the absorption edge allowed the bicomponent oxides to better utilize visible light, which also contributes to the high photocatalytic activity.

It is commonly accepted that well-structured mesopores and a large surface area make a superior photocatalyst, since more active adsorption sites are provided. The higher photoactivities of ZnO-CeO_2 photocatalysts compared to pure ZnO could be partly attributed to their special structural features and their high surface areas with smaller crystal sizes than those of pure ZnO and CeO_2, which is supported by N_2 sorption, XRD, and TEM analysis. The hydrangea-like morphology of the hierarchical meso-/macroporous structure would effectively prevent aggregation and thus maintain a large active surface area. Comparatively, unwanted aggregation during the reaction usually leads to a significant decrease in the active surface area and thus the photocatalytic performance of the reference samples, such as pure ZnO nanopowders.[39] On the other hand, the micro-/nanocomposite architecture could also increase the efficiency of photoabsorption and improve mass transfer.[42] It is well known that the photoabsorption efficiency is one of the main factors influencing the overall photocatalytic activity, which is strongly influenced by the pore wall structure of photocatalysts. In the macro-/mesoporous ZnO-CeO_2 photocatalysts, the macropores act as light-transfer paths for the distribution of photon energy onto the inner surface of the mesoporous materials, which allow the light waves to penetrate deep inside the photocatalyst, making it a more efficient light harvester. It is known that the original intensity of light at a wavelength of 320 nm is greatly weakened after penetrating a distance of only 8.5 μm into condensed TiO_2.[43] The presence of macrochannels or macrovoids, however, makes it possible to illuminate even the core of particles with the emission from surrounding light sources. The core mentioned here points to the inner surface of the hollow ZnO-CeO_2 clusters caused by the irregular macrovoids, which is distinct from the body of bulk materials. Thus the inner surface is also relevant to the photocatalysis, and macrovoids with a diameter of around 1 μm were large enough for the conduction of light. Reflection, scattering, and absorption of light take place in such a porous structure, which could enlarge the effective light-activated surface area, leading to an increase in photoabsorption efficiency.[42] It is notable that the well-structured porosity, which is confirmed by N_2 sorption analysis and electron microscopy images, could act as effective transport paths to facilitate mass transfer of RhB molecules to the light-activated surface, also leading to the enhanced photocatalytic activity.

Activity for CO Removal

Carbon monoxide (CO) is one of the main gaseous pollutants that is generally produced and released from the combustion of fossil fuel. For instance, during the cold start period of vehicles, a lot of carbon monoxide and hydrocarbons are generated because of the incomplete combustion of the fuel, and these are harmful to human health and to the environment. Catalytic oxidation of CO is an efficient way to control toxic emissions. CeO_2 is an important three-way catalyst that has been widely used in automobile exhaust systems.[19,44] ZnO is also used in components of heterogeneous catalysts or catalyst supports for catalytic oxidation reactions.[18,45] In comparison with the complex synthesis process and high cost of noble-metal loaded catalysts, the prepared mixed oxides of CeO_2-ZnO can be directly employed for catalytic oxidation of CO.

Figure 10 shows the hydrogen temperature programmed reduction (H_2-TPR) profiles of the synthesized Ce60Zn40, CeO_2, and ZnO materials. For pure ZnO, no obvious reduction peaks could be detected up to 800 °C, but for pure CeO_2, two reduction peaks at around 430 and 740 °C were observed, which are ascribed to the reduction of surface and bulk oxygen of CeO_2,[46] respectively. It was interesting to know that the two reduction peaks at 310 and 710 °C of the ZnO-CeO_2 mixed oxide shifted to lower temperatures remarkably relative to those of pure CeO_2, indicating the superior oxidation activity of the binary oxides. The CO conversion as a function of temperature by the synthesized materials is shown in Figure 11. The total conversion temperatures 270, 290, and 300 °C were observed for Ce60Zn40, Ce50Zn50, and Ce40Zn60, respectively (Table 1), while total conversion was achieved at 355 and over 380 °C for pure CeO_2 and ZnO, respectively, suggesting that CeO_2-ZnO catalysts have an obviously higher catalytic activity than pure CeO_2 and ZnO catalysts, which is consistent with the H_2-TPR results. The half CO conversion temperatures were 223, 239, and 253 °C for Ce60Zn40, Ce50Zn50, and Ce40Zn60, respectively.

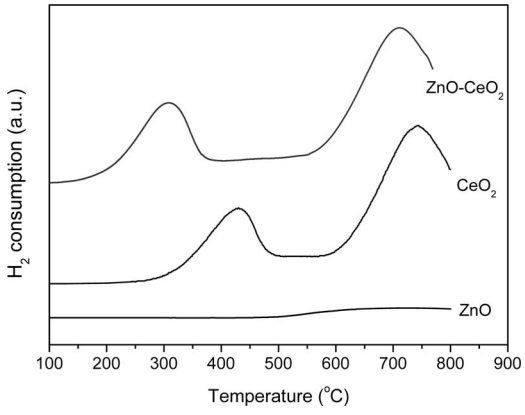

Figure 10. H_2-TPR profiles of the synthesized Ce60Zn40, CeO_2 and ZnO samples.

Because the physical and chemical properties of materials depend not only on the chemical composition but crucially also on their porosity and shape,[47] and there is general agreement that the catalytic process is mainly related to the adsorption and desorption of gas molecules on the surface of catalyst, much effort has been focused on tailoring the pore size and external morphology and enlarging the specific surface area of the catalysts. The large surface area, around 100 m^2/g, and the interconnected hydrangea-like hierarchical structure with small crystal size (ca. 5 nm) in our catalysts enable better contact with the gas molecules, and the coexistence of Ce^{4+} and Ce^{3+} on the surface of the

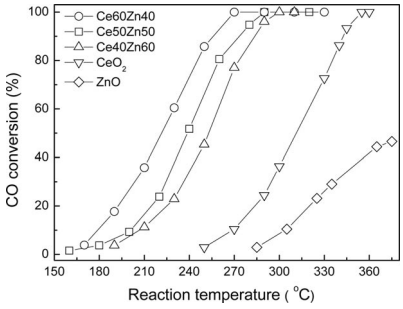

Figure 11. Catalytic activity for CO oxidation of the synthesized catalysts.

synthesized materials supplies plenty of reactive oxygen by releasing and uptaking oxygen through a redox process involving the Ce^{4+}/Ce^{3+} couple, which would further react with CO molecules adsorbed on the hierarchical materials to form CO_2. Therefore, the synthesized hierarchically structured CeO_2-ZnO materials reasonably exhibit better performance. Furthermore, the present mixed oxide materials could also be used as supports for base metals such as copper oxide, which can be expected to have promoted catalytic abilities.[37,47]

Conclusions

A new type of hierarchically structured CeO_2-ZnO materials has been prepared by a simple hydrothermal process with use of F127 as surfactant. The synthesized coupled CeO_2-ZnO materials possess a bicrystalline phase of wurtzite ZnO and cubic phase CeO_2 with a hydrangea-like morphology of hierarchical meso-/macroporous structure. It is believed that the F127 molecules not only assist the formation of micrometer-scaled macropores, but also direct the generation of mesostructure among the macroporous network. Coexistence of Ce^{3+} and Ce^{4+} on the surface of the ZnO-CeO_2 materials and a notable redshift of the absorption edge were observed, which would further contribute to the catalytic ability of the hierarchical bicomponent oxide catalysts. High photocatalytic activity for organic dye molecule degradation and efficient catalytic oxidation of CO were demonstrated, indicating the potential of the synthesized mixed oxide materials in environmental applications.

Experimental Section

Synthesis: Nonionic triblock copolymer F127 ($EO_{106}PO_{70}EO_{106}$) was obtained from Nanjing Well Chemical Co., and $Ce(NO_3)_3 \cdot 6H_2O$, $Zn(NO_3)_2 \cdot 6H_2O$, NaOH, and Rhodamine B (RhB) were obtained from Tianjin Kermel Chemical Co. All chemicals were used as received without further purification. In a typical synthesis procedure, F127 (2.0 g) was added into a mixture of deionized water (15 mL) and ethanol (15 mL). Different amounts of $Ce(NO_3)_3 \cdot 6H_2O$ and $Zn(NO_3)_2 \cdot 6H_2O$ were added into the solution, resulting in Ce/Zn molar ratios of 40:60, 50:50, and 60:40, which were marked as Ce40Zn60, Ce50Zn50, and Ce60Zn40, respectively. The pH value of the mixture was adjusted to 9–10 by addition of NaOH solution (0.6 mol/L). After a stirring further for 24 h, the mixture obtained was sealed in a Teflon-lined autoclave and aged statically at 110 °C for 48 h. The product was filtered, washed with water, and dried at 60 °C. Removal of the surfactant was accomplished by heating at 500 °C for 3 h in air. Pure ZnO and CeO_2 samples were also synthesized by a similar method for comparison.

Characterization: Scanning electron microscopy (SEM) and transmission electron microscopy (TEM) were carried out with a Shimadzu SS-550 microscope at 15 keV and a Philips Tecnai G20 instrument at 200 kV, respectively. N_2 adsorption/desorption isotherms were recorded with a Quantachrome NOVA 2000e sorption analyzer at liquid nitrogen temperature (77 K). The samples were degassed at 200 °C overnight prior to the measurements. The surface area was obtained by the Brunauer–Emmett–Teller (BET) method, and pore-size distribution was calculated from the adsorption branch of the isotherm by the Barret–Joyner–Halenda (BJH) model. X-ray diffraction (XRD) patterns were recorded with a Rigaku D/max-2500 diffractometer with Cu-K_α radiation operated at 40 kV and 100 mA. Diffuse reflectance UV/Vis. absorption spectroscopy was performed with a JASCO V-570 UV/Vis/NIR spectrophotometer over the wavelength range 200–800 nm, by using $BaSO_4$ as a reference. Thermogravimetry (TG) and differential scanning calorimetry (DSC) were performed by using a TA Q600 instrument at a heating rate of 5°/min with α-Al_2O_3 as the reference. X-ray photoelectron spectroscopy (XPS) measurements were performed with a Kratos Axis Ultra DLD (delay line detector) spectrometer equipped with a monochromatic Al-K_α X-ray source (1486.6 eV). All XPS spectra were recorded by using an aperture slot of 300×700 microns; survey spectra were recorded with a pass energy of 160 eV and high-resolution spectra with a pass energy of 40 eV.

Photocatalytic Activity Test: The photocatalytic activity experiments were performed by the degradation of RhB dye under either UV or visible light irradiation in air at room temperature. In the UV photocatalysis experiment, the synthesized catalyst (5.5 mg) was placed into a tubular quartz reactor of RhB aqueous solution (100 mL, 1×10^{-5} mol/L). A 125W UV lamp with maximum emission at 365 nm was located 10 cm higher than the solution surrounded by a circulating water tube. The reaction mixture was stirred under UV light irradiation. The mixture, sampled at different times, was centrifuged for 5 min to discard any sediment. The absorbance of reaction solutions was measured by a SP-722 spectrometer at λ_{max} = 554 nm. The visible light photodecomposition of RhB was carried out with a household desktop lamp with a 40-watt tungsten bulb as the visible light source, of which the wavelength range is usually considered to be 400–2500 nm, and the concentration of RhB solution and the amount of catalyst used were 1×10^{-5} mol/L and 20 mg, respectively. The activities of pure CeO_2 and ZnO were also investigated under identical conditions for comparison.

CO Removal Test: Catalytic activity tests were performed in a continuous-flow fixed-bed microreactor. A stainless steel tube with an inner diameter of 7 mm was chosen as the reactor tube. The synthesized catalyst powder (about 200 mg) was placed into the tube. The reaction gas mixture consisting of CO (10 vol.-%) balanced with air was passed through the catalyst bed at a total flow rate of 36.6 mL/min. A typical weigh hourly space velocity (WHSV) was 11,000 ml/h/g. After reaction for 30 min, the effluent gases were analyzed online with a GC-900A gas chromatograph equipped with a thermal conductivity detector. The activity was expressed by the conversion of CO.

Supporting Information (see footnote on the first page of this article): SEM images of uncalcined Ce50Zn50, pure ZnO and pure

CeO_2; pore width distribution curves of the synthesized samples, determined by the DFT method.

Acknowledgments

This work was supported by the National Natural Science Foundation of China (No. 20673060), the National Basic Research Program of China (No. 2009CB623502), the Specialized Research Fund for the Doctoral Program of Higher Education (20070055014), the Natural Science Foundation of Tianjin (08JCZDJC21500), the Chinese-Bulgarian Scientific and Technological Cooperation Project, the Ministry of Education (MOE) Supporting Program for New Century Excellent Talents (NCET-06–0215) and Nankai University.

[1] K. Nakagawa, Y. Murata, M. Kishida, M. Adachi, M. Hiro, K. Susa, *Mater. Chem. Phys.* **2007**, *104*, 30–39.
[2] K. H. Yoon, J. Cho, D. H. Kang, *Mater. Res. Bull.* **1999**, *34*, 1451–1461.
[3] R. J. Davis, Z. Liu, *Chem. Mater.* **1997**, *9*, 2311–2324.
[4] J. Shiyanovskaya, M. J. Hepel, *Electrochem. Soc.* **1999**, *146*, 243.
[5] F. X. Redl, K. S. Cho, C. B. Murray, S. O'Brien, *Nature* **2003**, *423*, 968–971.
[6] K. J. C. van Bommel, A. Friggeri, S. Shinkai, *Angew. Chem. Int. Ed.* **2003**, *42*, 980–999.
[7] A. Hernández, L. Maya, E. Sánchez-Mora, E. M. Sánchez, *J. Sol-Gel Sci. Technol.* **2007**, *42*, 71–78.
[8] D. Chen, H. Zhang, S. Hu, J. Li, *J. Phys. Chem. C* **2008**, *112*, 117–122.
[9] E. S. Toberer, J. D. Epping, B. F. Chmelka, R. Seshadri, *Chem. Mater.* **2006**, *18*, 6345–6351.
[10] M. Yuan, Z. Shan, B. Tian, B. Tu, P. Yang, D. Zhao, *Microporous Mesoporous Mater.* **2005**, *78*, 37–41.
[11] S. Ikeda, Y. Ikoma, H. Kobayashi, T. Harada, T. Torimoto, B. Ohtanic, M. Matsumura, *Chem. Commun.* **2007**, 3753–3755.
[12] S. G. Yang, X. Quan, X. Y. Li, Y. Z. Liu, S. Chen, G. H. Chen, *Phys. Chem. Chem. Phys.* **2004**, *6*, 659.
[13] J. Villasenor, P. Reyes, G. Pecchi, *J. Chem. Technol. Biotechnol.* **1998**, *72*, 105.
[14] B. Pal, M. Sharon, *Mater. Chem. Phys.* **2002**, *76*, 82.
[15] Y. Xu, H. Chen, Z. Zeng, B. Lei, *Appl. Surf. Sci.* **2006**, *252*, 8565–8570.
[16] J. Fang, X. Bi, D. Si, Z. Jiang, W. Huang, *Appl. Surf. Sci.* **2007**, *253*, 8952–8961.
[17] S. Pavasupreea, Y. Suzukia, S. Pivsa-Artb, S. Yoshikawa, *J. Solid State Chem.* **2005**, *178*, 128–134.
[18] S. Schuyten, P. Dinka, A. S. Mukasyan, E. Wolf, *Catal. Lett.* **2008**, *121*, 189–198.
[19] C. Ho, J. C. Yu, X. Wang, S. Lai, Y. Qiu, *J. Mater. Chem.* **2005**, *15*, 2193–2201.
[20] T. Z. Ren, Z. Y. Yuan, B. L. Su, *Chem. Commun.* **2004**, 2730–2731.
[21] P. Yang, T. Deng, D. Zhao, P. Feng, D. Pine, B. F. Chmelka, G. M. Whitesides, G. D. Stucky, *Science* **1998**, *282*, 2244–2246.
[22] A. Imhof, D. J. Pine, *Nature* **1997**, *389*, 948.
[23] K. Nakanishi, *J. Porous Mater.* **1997**, *4*, 67.
[24] T. Amatani, K. Nakanishi, K. Hirao, T. Kodaira, *Chem. Mater.* **2005**, *17*, 2114.
[25] T. Z. Ren, Z. Y. Yuan, A. Azioune, J. J. Pireaux, B. L. Su, *Langmuir* **2006**, *22*, 3886–3894.
[26] Z. Y. Yuan, B. L. Sun, *J. Mater. Chem.* **2006**, *16*, 663–677.
[27] Z. Y. Yuan, T. Z. Ren, A. Azioune, J. J. Pireaux, B. L. Su, *Chem. Mater.* **2006**, *18*, 1753–1767.
[28] Z. R. Shen, G. J. Zhang, H. J. Zhou, P. C. Sun, B. H. Li, D. T. Ding, T. H. Chen, *Adv. Mater.* **2008**, *20*, 984–988.
[29] M. Kruk, M. Jaroniec, *Chem. Mater.* **2001**, *13*, 3169–3183.
[30] S. Xu, Z. H. Li, Q. Wang, L. J. Cao, T. M. He, G. T. Zou, *J. Alloys Compd.* **2008**, *465*, 56–60.
[31] Y. S. Fu, X. W. Du, J. Sun, Y. F. Song, J. Liu, *J. Alloys Compd.* **2008**, *461*, 527–531.
[32] L. S. Zhong, J. S. Hu, A. M. Cao, Q. Liu, W. G. Song, L. J. Wan, *Chem. Mater.* **2007**, *19*, 1648–1655.
[33] M. C. Cabús-Llauradó, Y. Cesteros, F. Medina, P. Salagre, J. E. Sueiras, *Microporous Mesoporous Mater.* **2007**, *100*, 167–172.
[34] T. Y. Ma, X. J. Zhang, G. S. Shao, J. L. Cao, Z. Y. Yuan, *J. Phys. Chem. C* **2008**, *112*, 3090–3096.
[35] J. L. Blin, A. Léonard, Z. Y. Yuan, L. Gigot, A. Vantomme, A. K. Cheetham, B. L. Su, *Angew. Chem. Int. Ed.* **2003**, *42*, 2872–2875.
[36] H. F. Zhang, G. C. Hardy, M. J. Rosseinsky, A. I. Cooper, *Adv. Mater.* **2003**, *15*, 78.
[37] J. L. Cao, Y. Wang, T. Y. Zhang, S. H. Wu, Z. Y. Yuan, *Appl. Catal. B: Environ.* **2008**, *78*, 120–128.
[38] T. S. Jeong, J. H. Kim, S. J. Bae, C. J. Youn, *Cryst. Res. Technol.* **2008**, *43*, 289–292.
[39] F. Lu, W. P. Cai, Y. G. Zhang, *Adv. Funct. Mater.* **2008**, *18*, 1–10.
[40] F. Xu, P. Zhang, A. Navrotsky, Z. Y. Yuan, T. Z. Ren, M. Halasa, B. L. Su, *Chem. Mater.* **2007**, *19*, 5680–5686.
[41] S. X. Yang, W. P. Zhu, Z. P. Jiang, Z. X. Chen, J. B. Wang, *Appl. Surf. Sci.* **2006**, *252*, 8499–8505.
[42] X. C. Wang, J. C. Yu, C. M. Ho, Y. D. Hou, X. Z. Fu, *Langmuir* **2005**, *21*, 2552–2559.
[43] A. Hagfeldt, M. Grätzel, *Chem. Rev.* **1995**, *95*, 49–68.
[44] G. Z. Chen, C. X. Xu, X. Y. Song, W. Zhao, Y. Ding, S. X. Sun, *Inorg. Chem.* **2008**, *47*, 723–728.
[45] M. L. Cubeiro, J. L. G. Fierro, *J. Catal.* **1998**, *179*, 150–162.
[46] J. F. Chen, J. J. Zhu, Y. Y. Zhan, X. Y. Lin, G. H. Cai, K. M. Wei, Q. Zheng, *Appl. Catal. A: Gen.* **2009**, *363*, 208–215.
[47] J. L. Cao, Y. Wang, X. L. Yu, S. R. Wang, S. H. Wu, Z. Y. Yuan, *Appl. Catal. B: Environ.* **2008**, *79*, 26–34.

Received: October 9, 2009
Published Online: December 22, 2009

